

UCRL- 94309
PREPRINT

CIRCULATION COPY
SUBJECT TO RECALL
IN TWO WEEKS

USE OF DIGITAL IMAGE ANALYSIS TO
ESTIMATE FLUID PERMEABILITY OF POROUS MATERIALS
I. APPLICATION OF TWO-POINT CORRELATION FUNCTIONS

James G. Berryman
Stephen C. Blair

This paper was prepared for submittal to
Journal of Applied Physics

March 1986

Lawrence
Livermore
National
Laboratory

This is a preprint of a paper intended for publication in a journal or proceedings. Since changes may be made before publication, this preprint is made available with the understanding that it will not be cited or reproduced without the permission of the author.

DISCLAIMER

This document was prepared as an account of work sponsored by an agency of the United States Government. Neither the United States Government nor the University of California nor any of their employees, makes any warranty, express or implied, or assumes any legal liability or responsibility for the accuracy, completeness, or usefulness of any information, apparatus, product, or process disclosed, or represents that its use would not infringe privately owned rights. Reference herein to any specific commercial product, process, or service by trade name, trademark, manufacturer, or otherwise, does not necessarily constitute or imply its endorsement, recommendation, or favoring by the United States Government or the University of California. The views and opinions of authors expressed herein do not necessarily state or reflect those of the United States Government or the University of California, and shall not be used for advertising or product endorsement purposes.

**USE OF DIGITAL IMAGE ANALYSIS
TO ESTIMATE FLUID PERMEABILITY OF POROUS MATERIALS
I. APPLICATION OF TWO-POINT CORRELATION FUNCTIONS**

**James G. Berryman and Stephen C. Blair
Lawrence Livermore National Laboratory
University of California
P. O. Box 808 L-156
Livermore, CA 94550**

ABSTRACT

Scanning electron microscope images of cross sections of several porous specimens have been digitized and analyzed using image processing techniques. The porosity and specific surface area may be estimated directly from measured two-point spatial correlation functions. The measured values of porosity and specific surface area were combined with known values of electrical formation factors to estimate fluid permeability using one version of the Kozeny-Carman empirical relation. For glass bead samples with measured permeability values in the range of a few darcies, our estimates agree well ($\pm 10\text{-}20\%$) with the measurements. For samples of Ironton-Galesville sandstone with a permeability of similar magnitude, our results agree with the laboratory measurements well within an order of magnitude. For Berea sandstone with much lower permeability (tens of millidarcies), our predictions from the images are again quite good.

I. INTRODUCTION

Fluid permeability is an important physical property of porous materials with connected void space. The rate at which a viscous fluid will flow through such a porous medium is proportional to the pressure gradient, and the constant of proportionality is called Darcy's constant, or the permeability k . This constant k is probably most important for studies of ground water flow and oil field engineering, but it also arises in medicine and in biochemical and electrochemical engineering through various applications of permeable membranes.¹ For hydrological and oil field applications, direct measurement of the permeability is both difficult and expensive since it may require forcing a fluid through a large bulk of porous earth. Thus, a simple and cheap indirect measurement of k , even if it is of only modest accuracy, is highly desirable. The purpose of this paper is to present such a method based on an analysis of the surface topology of porous rocks using image processing techniques.

Four principal methods of analyzing permeability have been developed in the century following the discovery² of Darcy's law: (1) empirical methods associated with the names of Kozeny and Carman,³ (2) effective medium methods associated with the name of Brinkman,⁴ (3) network modelling methods first introduced by Fatt,⁵⁻⁷ and (4) variational methods first introduced by Prager.⁸⁻¹⁰

The empirical methods are generally based on very simple formulas derived using cylindrical tube models for the pores. The empiricism enters through constant scale factors that are chosen to fit data.¹¹ Walsh and Brace¹² recently reexamined this approach and, in the same spirit, obtained a formula relating permeability to porosity, formation factor, and specific surface area. They found their formula provided a good means of correlating data on permeability and formation factor for low-porosity, low-permeability granites. We will have more to say about this approach later in this paper.

None of the other methods for analyzing permeability seems to work as well as the purely empirical approach. For example, Brinkman's effective medium approach has recently been reexamined by Wilkinson,¹³ who found only order of magnitude agreement between theory and experiment. Similarly, Wong et al.¹⁴ and Koplik et al.¹⁵ have attempted to combine network models with effective medium estimates and again obtained only order of magnitude agreement. Finally, Berryman and Milton¹⁶ reexamined the variational methods with the result that, for those cases where the needed spatial correlation functions were available, the agreement between theory and experiment was no better than order of magnitude in the porosity range of practical interest. Despite the sophistication of all of these methods, the results obtained using them are quite disappointing.

The approach to be presented in this paper is a hybrid. From the variational methods, we take the idea of measuring the statistical properties of the porous material^{17,18} using image processing techniques.¹⁹ Then, rather than using this information in the variational

bounds (which would only provide order of magnitude agreement), we use these results as input to the empirical formula derived by Walsh and Brace.¹² As we will show, the results obtained in this manner are surprisingly good for the various sandstones and glass bead samples used in the experiments.

In Section II, we define the correlation functions and show how the relevant physical parameters are determined by them. In Section III, we present a discussion of the specific Kozeny-Carman empirical relationship to be used in the remainder of the paper. Section IV describes our experimental methods, and Section V our results. Section VI summarizes our conclusions.

II. SPATIAL CORRELATION FUNCTIONS

A discussion of the significance of the spatial correlation functions has been presented recently, together with a detailed analysis of methods for obtaining these functions experimentally using image processing techniques.¹⁹ We will not repeat the detailed discussion here, but it is still necessary to define the correlation functions and mention their relevant properties.

For a porous material, we define a characteristic function $f(\vec{x}) = 0$ or 1 . Then, we say that void regions have $f = 1$, while material regions have $f = 0$. The first three void-void correlation functions are then given by

$$\hat{S}_1 = \langle f(\vec{x}) \rangle = \phi, \quad (1)$$

$$\hat{S}_2(\vec{r}_1, \vec{r}_2) = \langle f(\vec{x} + \vec{r}_1) f(\vec{x} + \vec{r}_2) \rangle, \quad (2)$$

and

$$\hat{S}_3(\vec{r}_1, \vec{r}_2, \vec{r}_3) = \langle f(\vec{x} + \vec{r}_1) f(\vec{x} + \vec{r}_2) f(\vec{x} + \vec{r}_3) \rangle. \quad (3)$$

The brackets $\langle \cdot \rangle$ indicate a volume average over the spatial coordinate \vec{x} . The void volume fraction (or porosity) is given by ϕ . We will refer to the three correlation functions defined above as the one-, two-, and three-point correlation functions, respectively. Since two points lie along a line and three points lie in a plane, the two-point and three-point correlations (as well as the one-point correlation) may be measured by processing images of material cross sections. In the present paper, we will stress the one- and two-point correlation functions; however, the three-point correlation functions can also be obtained from these same pictures and will be pursued in detail in a later publication. In general, we assume that the porous medium of interest is statistically homogeneous so that on average only the differences in the coordinate values are significant (translational invariance). Furthermore, we often assume that the material is at least locally isotropic so that the averages do not depend on orientation of the arguments. With these assumptions, we find that the two-point correlation function simplifies to

$$\hat{S}_2(\vec{r}_1, \vec{r}_2) = \tilde{S}_2(\vec{r}_2 - \vec{r}_1) = S_2(|\vec{r}_2 - \vec{r}_1|). \quad (4)$$

Various facts about the correlation functions are quoted in Ref. 19. The most important ones for the present application of two-point correlation functions are, in the isotropic case with $r = |\vec{r}|$,

$$S_2(0) = \phi, \quad (5)$$

$$\lim_{r \rightarrow \infty} S_2(r) = \phi^2, \quad (6)$$

and

$$S_2'(0) = -s/4, \quad (7)$$

where s is the specific surface area (internal surface area per unit volume). The important theorem stated in Eq. (7) concerning the relationship between the two-point correlation function and the specific surface area has been known since the work of Debye et al.²⁰, and can be derived fairly simply from its definition. To see this, consider

$$S_2(r) = \frac{1}{V} \int_V d^3x f(\vec{x}) f(\vec{x} + \vec{r}), \quad (8)$$

where V is total volume of integration. Since Eq. (8) is independent of the direction of \vec{r} , it is convenient to average (8) over all angles according to

$$S_2(r) = \frac{1}{4\pi V} \int d\varphi d\theta \sin \theta \int_V d^3x f(\vec{x}) f(\vec{x} + r\hat{r}), \quad (9)$$

where $\hat{r} = \hat{r}(\theta, \varphi)$ is the radial unit vector. Taking the derivative of S_2 then gives

$$\frac{dS_2(r)}{dr} = \frac{1}{4\pi V} \int d\varphi d\theta \sin \theta \int_V d^3x f(\vec{x}) \frac{\partial f(\vec{x} + r\hat{r})}{\partial r}. \quad (10)$$

Defining the pore volume as V_p and skipping some intermediate steps in the calculation, we have

$$\frac{dS_2(r)}{dr} = \frac{1}{4\pi V} \int d\varphi d\theta \sin \theta \hat{r} \cdot \int_{V_p} d^3x \vec{\nabla} f(\vec{x} + r\hat{r}). \quad (11)$$

Then, if da_s is an infinitesimal element of the material surface area A_s , we have

$$\frac{dS_2(r)}{dr} = \frac{1}{4\pi V} \int_{A_s} da_s \int d\varphi d\theta \sin \theta \hat{r} \cdot \hat{n}_s f(\vec{x}_s + r\hat{r}), \quad (12)$$

where \hat{n} is the unit outward normal vector at the surface position given by \vec{x}_s . Now, if we let $r \rightarrow 0^+$ and center the coordinate system at \vec{x}_s with $\hat{n} = \hat{z}$, we find that

$$\int d\varphi d\theta \sin \theta \hat{r} \cdot \hat{n}_s f(\vec{x}_s + 0^+\hat{r}) = 2\pi \int d\theta \sin \theta \cos \theta f(\vec{x}_s + 0^+\hat{r}) = 2\pi \int_{-1}^0 d\mu \mu = -\pi \quad (13)$$

and we obtain a definite result for Eq. (12) given by

$$\lim_{r \rightarrow 0^+} \frac{dS_2(r)}{dr} = -\frac{A_s}{4V}. \quad (14)$$

Since the specific surface area is defined as $s = A_s/V$, Eq. (14) is equivalent to Eq. (7). Debye et al.²⁰ used a more intuitive approach to obtain the same result.

Figure 1 shows two-point correlation functions calculated²¹⁻²³ for assemblages of hard and soft spheres and emphasizes the relevant aspects of the function that will be used in the subsequent analysis.

III. FLUID PERMEABILITY

Walsh and Brace¹² recently used a cylindrical tube model of pore structure to derive a formula relating permeability to porosity, formation factor, and specific surface area. These authors found that their formula provided a good means of correlating data on permeability and formation factor for low-porosity, low-permeability granites. Their formula has the general form

$$k_{KC} = \frac{\phi^2}{bF_s^2}, \quad (15)$$

where b is a constant that depends on the cross section of the tubes. Approximate formulas such as Eq. (15) are well known in the study of permeability, and we will refer to all such formulas as Kozeny-Carman relations. In version (15) of the Kozeny-Carman relation, the electrical formation factor F (i.e., the electrical conductivity of a conducting pore fluid divided by the effective electrical conductivity of the saturated porous insulating material) supplies a measure of the tortuosity of the connected pore space. The remaining term b is a weak function of the shape of the tubes in the model used to derive the formula. Typically, $b = 2$ for circular tubes and $b = 3$ for flat cracks. In the present work, we have used the fixed value of $b = 2$ throughout.

Although Eq. (15) was derived under fairly restrictive assumptions concerning the structure of the pore space, this formula has one very appealing feature that is not always shared by other versions of the Kozeny-Carman relation: Except for the nearly constant structure-dependent factor b , all quantities appearing in the formula have a well-defined physical meaning and can, in principle, be measured independently of the permeability and of each other. By contrast, approximate formulas quoted in terms of the "hydraulic radius" must provide independent means both for defining and for measuring this quantity in porous materials with tortuous, meandering pathways of variable cross-section.^{1,11,24}

To establish a connection between the empirical formula in Eq. (15) and the variational bounds, and to provide another motivation for using Eq. (15), we will now show how the form of Eq. (15) can be inferred from the rigorous two-point bounds on permeability. Berryman and Milton¹⁶ have shown that a rigorous bound on the permeability of a porous material is given by

$$k \leq \frac{2}{3} \frac{\int_0^\infty dr r [S_2(r) - \phi^2]}{(1 - \phi)^2}. \quad (16)$$

To evaluate the integral in Eq. (16), we will make a crude approximation to the two-point correlation function. It follows from Eqs. (5)-(7) that for small r , the two-point correlation function is given approximately by

$$S_2(r) = \phi - \frac{1}{4}sr, \quad (17)$$

whereas for large r , it is given by

$$S_2(r) = \phi^2. \quad (18)$$

The straight lines defined in Eqs. (17) and (18) intersect at the point

$$r_c = \frac{4\phi(1-\phi)}{s}. \quad (19)$$

Thus, if we extrapolate both Eqs. (17) and (18) beyond their strict range of validity using Eq. (17) for all $r \leq r_c$ and Eq. (18) for all $r \geq r_c$, then the integral in Eq. (16) may be approximated as

$$\int_0^{r_c} dr r [\bar{S}_2(r) - \phi^2] = \frac{8}{3} \frac{\phi^3 (1-\phi)^3}{s^2}. \quad (20)$$

The resulting crude estimate of the bound on permeability is

$$k \leq \frac{16}{9} \frac{\phi^2}{s^2} \phi(1-\phi). \quad (21)$$

For comparison, consider the limit of very high porosity ($\phi \rightarrow 1$). In this limit, the formation factor is known to approach unity. Using the well-known results for Stokes flow around spherical particles, the effective permeability is then given by

$$k = \frac{2}{9} \frac{R^2}{(1-\phi)}, \quad (22)$$

where R is the radius of the spheres and the number density n is related to the porosity by $\frac{4\pi}{3} n R^3 = 1 - \phi$. The specific surface area is given by $s = 4\pi n R^2 = 3(1-\phi)/R$, so (22) can be rewritten as

$$k = \frac{2}{s^2} (1-\phi), \quad \text{as } \phi \rightarrow 1. \quad (23)$$

Thus, we see that Eqs. (21) and (23) agree in this limit within a factor of $\frac{8}{9}$. This agreement is surprisingly good considering how crudely S_2 has been approximated. The Kozeny-Carman relation in Eq. (15) does not perform well in this regime. At high porosity, the formation factor approaches unity and Eq. (15) therefore diverges like $(1-\phi)^{-2}$, whereas the exact result for spheres in Eq. (22) diverges like $(1-\phi)^{-1}$ in this limit. We conclude that Eq. (15) as written is certainly a valid approximation only for lower porosities, and we would argue that it should not be used without modification for porosities $\phi \geq 0.50$.

In the opposite limit of very low porosity ($\phi \rightarrow 0$), it is known that the two-point variational bound cannot provide a close estimate of the permeability.²⁵ [Some positive terms with significant values on the left hand side of (16) have been neglected in its

derivation.] To analyze Eq. (15) in the low porosity limit, we first note that a rigorous bound on the formation factor F is given by the Hashin-Shtrikman bound^{26,27}

$$\frac{1}{F} \leq \frac{2\phi}{(3 - \phi)}. \quad (24)$$

Then, as $\phi \rightarrow 0$, Eq. (15) is no larger than

$$k_{KC}^+ = \frac{\phi^3}{3s^2}, \quad (25)$$

while Eq. (21) reduces to

$$k \leq \frac{16}{9} \frac{\phi^3}{s^2}. \quad (26)$$

We see that the functional form is the same for Eqs. (25) and (26), but that they differ by a factor of $\frac{16}{3}$. Although the quantitative agreement is only order of magnitude, the qualitative agreement between Eqs. (15) and (16) is therefore quite good in this limit.

These calculations demonstrate a weak connection between the two-point variational bound in Eq. (16) and the empirical formula in Eq. (15). We emphasize that the formula in Eq. (15) is only an approximation, derived assuming that the pore space is well-characterized by a network of tubes with simple connectedness properties. We have shown that these assumptions are certainly violated for high-porosity materials. Nevertheless, we have applied Eq. (15) to the porous materials considered in this paper because, even though it is imperfect, we have found that Eq. (15) does seem to capture several of the key features of the relationship between permeability and formation factor.

IV. EXPERIMENTAL METHODS

Digital images of the microstructure of materials used in this study were produced as follows: First, samples of the materials were vacuum-impregnated with low viscosity epoxy, and then standard petrographic thin sections were prepared. The thin sections were uncovered and polished with $\frac{1}{4}$ micron diamond grit. A scanning electron microscope (SEM) was used in backscatter mode to view the sections and to produce high contrast images of the pore and grain structure of the sections. These images were recorded as black and white negatives using Polaroid film. Images were produced at magnifications between $20\times$ and $2000\times$. The photographic negatives (3 in. \times 4 in.) were digitized using a raster scanning digitizer, and the raw digital images were stored on disk as 512×512 arrays. This procedure is presented schematically in Figure 2.

The raw digital images were processed using a series of digital image processing techniques. First, a working image was formed by extracting a square (*e.g.*, $400 \text{ pixel} \times 400 \text{ pixel}$) portion of the microstructure contained in the raw image and translating this area into a 512×512 array, using a bilinear mapping. The true scale of this working image (micron/pixel) was computed using the SEM scale reference bar. A histogram of the array values for the working image was also obtained. The next step was to create an image of zeros and ones that closely approximated the grain and pore structure of the working image. This "binary" image was produced using a simple thresholding technique in which the threshold was determined interactively by the operator, using the histogram and a video display that afforded direct comparison of the thresholded image to the original working image. Once an appropriate threshold was chosen, all pixels below the threshold were set to zero (grain) and all pixels above the threshold were set to one (pore). Computer processing of the image is shown schematically in Figure 3. A typical raw image produced from the SEM together with the corresponding histogram and binary image for glass beads are shown in Figure 4.

The autocorrelation function for each binary image was calculated using an array processor following the method described by Berryman.¹⁹ The two-point spatial correlation function (S_2) is easily found from the autocorrelation function and plotted as shown in Figure 4(c). A line was fitted to the first few (*e.g.*, five) points of S_2 and the slope of this line was used to determine the specific surface area following Eq. (7).

V. RESULTS

Glass Bead Samples

For glass bead samples, we analyzed images with 50 \times and 78 \times magnification. The 50 \times image is shown in Figure 4(a) and the resulting correlation function is shown in Figure 4(d). Note that the shape of the function is very similar to the theoretical function for the hard sphere model plotted in Figure 1. From the correlation function for both the 50 \times and 78 \times images, we estimate a mean sphere radius for the material of 65 - 70 microns. This estimate agrees semiquantitatively with measurements of the largest spheres made on the raw images. Thus, for the glass bead material, the correlation behaves as expected, indicating that the technique is producing appropriate results. From the two correlation functions, we estimated porosities of 35 and 43% for this material, which is somewhat higher than the value of 30% supplied by the manufacturer. The specific surface area was estimated to be 0.0241 and 0.0281 micron. These values were determined from the slope of the correlation function near zero, as shown in Figure 4(d). Using these values for porosity and specific surface area and Eq. (15) with $b = 2$, we predict the permeability of this material to be 9.7 - 10.7 darcy, which is very close to the laboratory value of 8.7 darcy supplied by the manufacturer. The above data are summarized in Table 1.

Ironton-Galesville Sandstone

The second material we applied this method to was Ironton-Galesville sandstone²⁸. This is a friable, medium-grained quartz sand with weak dolomitic cement. The two samples studied contained some clay-rich zones and shale interbeds. We analyzed a series of images with magnifications of 20 \times - 100 \times and typical images of areas with and without clay in the pore space are shown in Figures 5(a) and 6(a). Two-point correlation functions for these two images are presented in Figures 5(b) and 6(b). Note that, for the regions without much clay in the pore space, the correlation functions resemble the hard-sphere model; for regions with significant clay in the pore space, the correlation functions resemble a soft-sphere model. Particle size for each image was estimated from the corresponding correlation function, and (as for the glass beads) this estimate appears to be a semiquantitative measure of the size of the largest grains in the image. For images of sample IG-775 and IG-785, we measured porosities of 32 - 43% and 26 - 33% respectively. Unfortunately, laboratory porosity data are unavailable for these samples. Specific surface area was also estimated for these samples and values range from 0.0322 to 0.0924 micron (Table 1). As discussed above, we computed a permeability for each image using the corresponding porosity and specific surface area values. For these samples, the permeability estimates for 100 \times images show the best agreement with laboratory values. For sample IG-775, our estimated permeability is about a factor of 4.5 too high, except for one image of a clay-rich region (Figure 6). The estimated permeability for this image is only a factor of 1.5 too high,

and note that the specific surface area for this image is much higher than that measured for other regions. This apparent discrepancy is due to the large amount of fine-grained (clay) material in the image, and is consistent with the general observation that clay rich regions have lower permeability. Moreover, it is interesting to note that the worst estimate (7.7 darcy from image IG-775- $\times 20$) is still only an order of magnitude greater than the laboratory data. For comparison, note that order of magnitude agreement is typical for the currently available variational bounds as well as for other estimation methods.

Berea Sandstone

We also analyzed thin sections of Berea sandstone that were made from a sample which had been characterized in the laboratory by Daily and Lin.²⁰ They report that this Berea sandstone is 97% quartz, 2% potassium feldspar, and 1% other minerals. This is a well-cemented and well-sorted sandstone. For this sample, we studied images with magnifications of 50 \times , 100 \times , 200 \times , 490 \times , and 1000 \times . Typical images at 100 \times magnification are shown in Figures 7 and 8, along with their respective correlation functions. Note that, as with the Ironton-Galesville sandstone, the regions with clay in the pores produced correlation functions resembling the soft-sphere model, whereas the regions with little or no clay or other pore filling material produced correlation functions resembling the hard-sphere model. Daily and Lin report a porosity of 16-18% for this sample, and our estimates of porosity from images at 50 \times to 200 \times all fall within this range. Our estimate of particle size was also very consistent for these images, indicating that the largest particle size was in the range of 150 - 170 microns, again in semiquantitative agreement with observed particle size.

We estimated the specific surface area for the Berea sample from images with magnifications of 490 \times and 1000 \times ; the image at 490 \times is shown in Figure 9, along with the correlation function. The formation factor quoted in Table 1 for Berea is taken from a table in Dullien.¹ The 1000 \times image and its correlation function are shown in Figure 10(a) and (b). Note the distinct break in slope that occurs at lags of less than 3 microns in both Figures 9(b) and 10(b). This break indicates that features along grain boundaries are in this size range, and that they control the specific surface area. Similar values of s were predicted using both 490 \times and 1000 \times images, which were much higher than the values predicted using 100 \times and 200 \times images. Also note the linear decrease in the correlation function that occurs in the range of 2-12 microns at both 490 \times and 1000 \times magnification. This range of sizes coincides with that of the pore throats seen in each image and could be a useful measure of throat size. To predict permeability for this rock, we used the porosity value determined from the images at 50 \times - 200 \times and the specific surface area determined from images at 490 \times and 1000 \times . Our estimates of 16 and 18 mD are quite close to Daily and Lin's laboratory measurement of 23 mD. This result shows surprisingly

good agreement between the predictions and the laboratory measurements.

VI. CONCLUSIONS

In summary, we have used digital image analysis to calculate the two-point correlation functions and to estimate porosity and specific surface area for three very different porous materials. Porosity of the samples was determined from the images and these data were compared with porosity values previously determined in the laboratory. We found that porosity measured from images of $50\times$ - $200\times$ agreed well with laboratory values. However, images of this magnification were not adequate to compute specific surface area, because features smaller than a few microns were poorly resolved in the digitized images. (Table 1 shows that, as magnification is increased, the measured value of the specific surface area also tends to increase. To obtain information about features smaller than a few microns, images with the higher magnifications have to be studied.) For the present application, the glass bead samples were nearly ideal: The SEM images for glass were relatively easy to interpret, so the choice of threshold to produce the final binary image was not complicated. Furthermore, the range of particle sizes was narrow for the glass beads, so a single choice of magnification for the images (around $100\times$) proved adequate for all of the analyses.

By contrast, it was necessary to use several different magnifications for the sandstones, because the particle size distribution was quite broad. We found that for the Berea sandstone studied, magnification of $500\times$ - $1000\times$ produced consistent measurements of specific surface area. Our estimates of porosity agreed well with available laboratory measurements and, more importantly, our estimates of permeability (calculated using a Kozeny-Carman relation) also agreed well with measured values. Finally, we noticed that, for the sandstone samples, the amount of pore-filling material (such as clay) influenced the shape of the correlation function; it may therefore be possible to estimate other useful parameters such as mean pore throat size and mean particle size from the correlation function.

Although the results in the present paper are encouraging, we need to mention again the fact that laboratory data on the formation factor and specific surface area for the samples studied are sparse or lacking. In principle, the formation factor can be estimated from the SEM images in a manner analogous to that presented here by obtaining the three-point correlation function [Eq.(3)] of the sample surfaces and then using it to calculate the known variational bounds for electrical conductivity.¹⁷ This approach will be explored in detail in the second paper of this series.

Finally, it seems remarkable that an approximate formula like Eq. (15) should provide such good agreement with experiments over such a wide range of permeability. Walsh and Brace¹² showed that it worked well for granites with permeabilities in the nD range. The present study shows that it also works well for high-permeability sandstones. It is

therefore tempting to speculate that some deeper significance might be established for this particular Kozeny-Carman relation (or a slightly modified version of it) by studying rigorous relationships between k and F .

ACKNOWLEDGEMENTS

We thank B. P. Bonner for supplying the glass bead specimens used in this work and also for his measurements of the formation factors for these samples; W. D. Daily and W. Lin for supplying specimens of the Berea sandstone used in their experiments; J. M. Beiriger for able technical assistance in obtaining and processing SEM images. Work performed under the auspices of the U. S. Department of Energy by the Lawrence Livermore National Laboratory under contract No. W-7405-ENG-48 and supported specifically by the Institutional Research and Development Program within the Earth Sciences Department.

REFERENCES

1. F. A. L. Dullien, *Porous Media - Fluid Transport and Pore Structure* (Academic Press, New York, 1979), pp. 159-161.
2. H. Darcy, *Les fontaines publique de la ville de Dijon*, Paris, 1856.
3. P. C. Carman, *Flow of Gases through Porous Media* (Academic Press, New York, 1979), Sect. 8.2.
4. H. C. Brinkman, *Appl. Sci. Res. A* **1**, 27 (1947).
5. I. Fatt, *Trans. AIME* **207**, 144 (1956).
6. I. Fatt, *Trans. AIME* **207**, 160 (1956).
7. I. Fatt, *Trans. AIME* **207**, 164 (1956).
8. S. Prager, *Phys. Fluids* **4**, 1477 (1961).
9. H. L. Weissberg and S. Prager, *Phys. Fluids* **5**, 1390 (1962).
10. H. L. Weissberg and S. Prager, *Phys. Fluids* **13**, 2958 (1970).
11. J. R. Schopper, in *Physical Properties of Rocks, Vol. a*, edited by G. Angenheister (Springer-Verlag, Berlin, 1982), pp. 278-303.
12. J. B. Walsh and W. F. Brace, *J. Geophys. Res.* **89**, 9425 (1984).
13. D. Wilkinson, *Phys. Fluids* **28**, 1015 (1985).
14. P. Wong, J. Koplik, and J. P. Tomanic, *Phys. Rev. B* **30**, 6606 (1984).
15. J. Koplik, C. Lin, and M. Vermette, *J. Appl. Phys.* **56**, 3127 (1984).
16. J. G. Berryman and G. W. Milton, *J. Chem Phys.* **83**, 754 (1985).
17. M. J. Beran, *Statistical Continuum Theories* (Interscience, New York, 1968), Chapt. 6.
18. P. B. Corson, *J. Appl. Phys.* **45**, 3159 (1974).
19. J. G. Berryman, *J. Appl. Phys.* **57**, 2374 (1985).
20. P. Debye, H. R. Anderson, Jr., and H. Brumberger, *J. Appl. Phys.* **28**, 679 (1957).
21. S. Torquato, *Ph.D. Thesis* (State University of New York at Stony Brook, 1980), unpublished.
22. J. G. Berryman, *J. Comput. Phys.* **52**, 142 (1983).

23. S. Torquato and G. Stell, *J. Chem. Phys.* **82**, 980 (1985).
24. M. S. Paterson, *Mech. Mater.* **2**, 345 (1983).
25. J. G. Berryman, in *Proceedings of the Workshop on Homogenization and Effective Moduli of Materials and Media*, Institute for Mathematics and Its Applications, University of Minnesota, Minneapolis, MN, October 22-26, 1984, (Springer-Verlag, Berlin, 1986), in press.
26. Z. Hashin and S. Shtrikman, *J. Mech. Phys. Solids* **11**, 127 (1963).
27. J. G. Berryman, *Phys. Rev. B* **27**, 7789 (1983).
28. S. C. Blair, in *Proceedings of ENERSTOK '85, International Conference on Energy Storage for Building Heating-Cooling*, Toronto, Canada, Sept. 22-26, 1985 (Public Works, Canada, Ottawa, Canada).
29. W. D. Daily and W. Lin, *Geophysics* **50**, 775 (1985).

Table 1. Comparison of porosity and permeability values produced in this study with those obtained from laboratory measurements. The formula used for the permeability value obtained from the image in all cases was $k_{KO} = \phi^2/2Fs^2$. Formation factor values quoted in parentheses were estimated, not measured.

Sample	Magnification	Number of images	Specific surface area $s(\mu m^{-1})$	Porosity ϕ		Permeability $k(D)$		Formation factor F
				Image	Laboratory	Image	Laboratory	
Glass beads (55 μm)	50	1	0.0241	0.35	0.30	9.7	8.7	10.9
	78	1	0.0281	0.43	0.30	10.7	8.7	10.9
Ironton Galesville sandstone								
IG-775	20	1	0.0322	0.40	—	7.7	0.75 ^a	(10)
IG-775	50	1	0.0449	0.35	—	3.1	0.75 ^a	(10)
IG-775	100	3	0.0609	0.39	—	2.1	0.75 ^a	(10)
IG-785	100	3	0.0455	0.30	—	2.2	1.00 ^a	(10)
Berea	100	2	0.0281	0.17	0.15-0.18 ^b	0.312	0.023 ^b	62 ^c
Berea	200	1	0.0354	0.18	0.15-0.18 ^b	0.197	0.023 ^b	62 ^c
Berea	490	1	0.1167	0.224	0.15-0.18 ^b	0.018	0.023 ^b	62 ^c
Berea	1000	1	0.1231	0.393	0.15-0.18 ^b	0.016	0.023 ^b	62 ^c

^aRef. 28, ^bRef. 29, ^cRef. 1

Figure Captions

Figure 1. Two-point correlation functions for model materials composed of hard and soft spheres (modified from Ref. 21 with the author's permission). Quantities that can be determined directly from the shape of the two-point correlation functions include: (1) porosity, (2) specific surface area, and (3) mean particle size.

Figure 2. Schematic of image production methodology.

Figure 3. Schematic of digital image processing technique used to produce two-point correlation functions.

Figure 4. Glass bead example: (a) raw image, (b) histogram, (c) binary image, and (d) two-point correlation function. In 4(d), the dashed line is the least squares fit to the average value of S_2 ; the solid line is the average value of S_2 ; the other two curves (dot-dash and long-dash) are individual measurements of S_2 in two orthogonal directions which provide a measure of the anisotropy of the sample.

Figure 5. Ironton-Galesville sandstone IG-785 (without much clay): (a) SEM image and (b) two-point correlation function. In 5(b), the solid line is the measured average value of S_2 ; the dashed line is the analytical value of S_2 for a penetrable sphere model with the same porosity and specific surface area.

Figure 6. Ironton-Galesville sandstone IG-775 (with fine-grained material in the pores): (a) SEM image and (b) two-point correlation function. In 6(b), the solid and dashed lines have the same significance as in 5(b).

Figure 7. Berea sandstone (without substantial clay): (a) SEM image and (b) two-point correlation function. In 7(b), the solid and dashed lines have the same significance as in 5(b).

Figure 8. Berea sandstone (some pores filled with clay or fine-grained material): (a) SEM image and (b) two-point correlation function. In 8(b), the solid and dashed lines have the same significance as in 5(b).

Figure 9. Berea sandstone at 490 \times magnification: (a) SEM image and (b) two-point correlation function. In 9(b), the dashed line is the least squares fit to the average value of S_2 and the solid line is the average value of S_2 .

Figure 10. Berea sandstone at 1000 \times magnification: (a) SEM image showing grain edges and (b) two-point correlation function. In 10(b), the solid and dashed lines have the same significance as in 9(b).

Figure 1

2 point correlation function for impenetrable and fully penetrable spheres

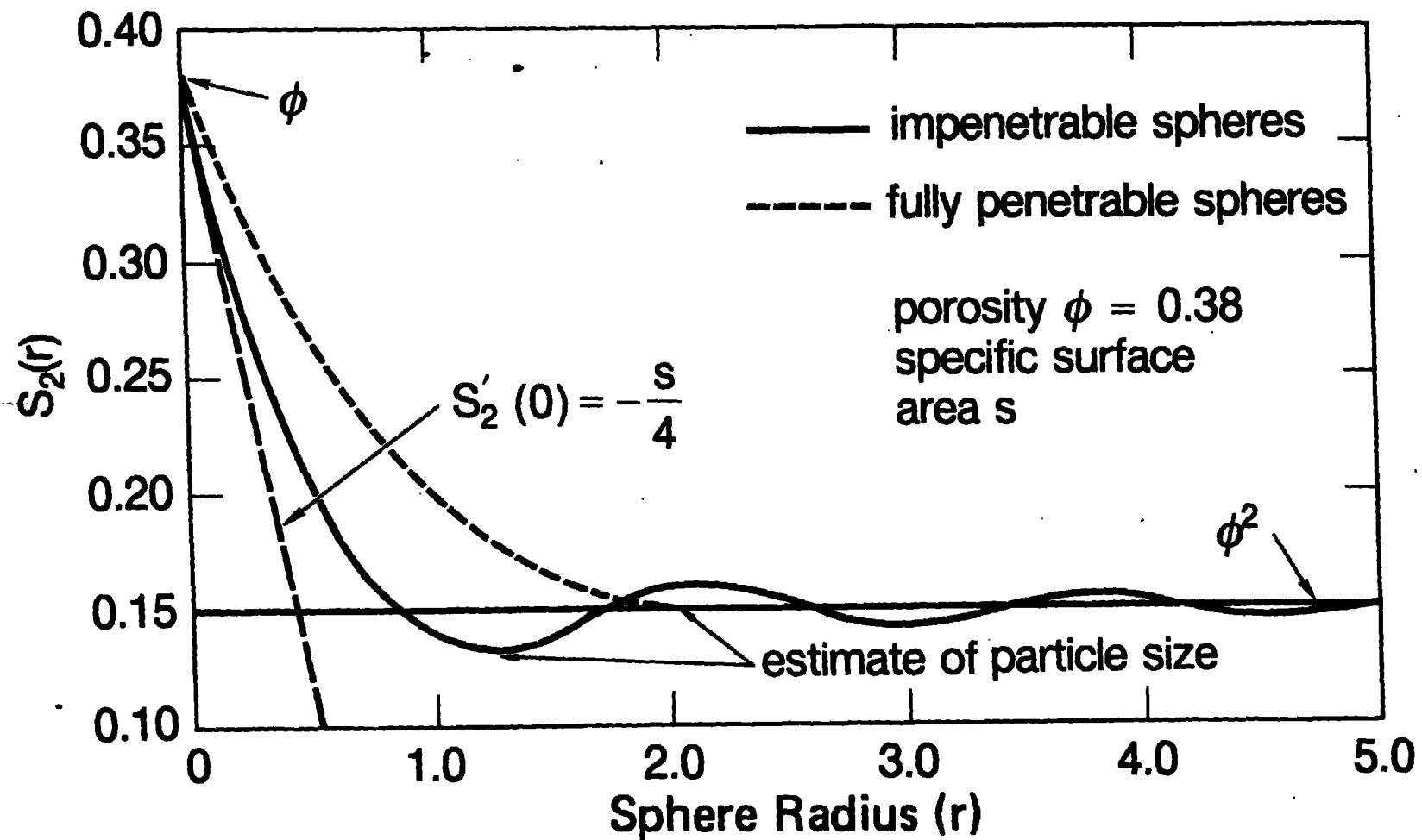


Figure 2

Standard epoxy impregnated thin sections produced from sandstone and glass bead samples.



Rock sample



Epoxy
impregnated
thin section

High contrast images of pore structure produced on scanning electron microscope (SEM). The SEM was used in backscatter mode and the images were recorded as photographic negatives.



SEM analysis



Photographic
negative

The raw images were digitized using an Eikonix scanning digitizer and stored on disk as digital arrays.



Eikonix scanning
digitizer



Digital image file
on disk

Figure 3

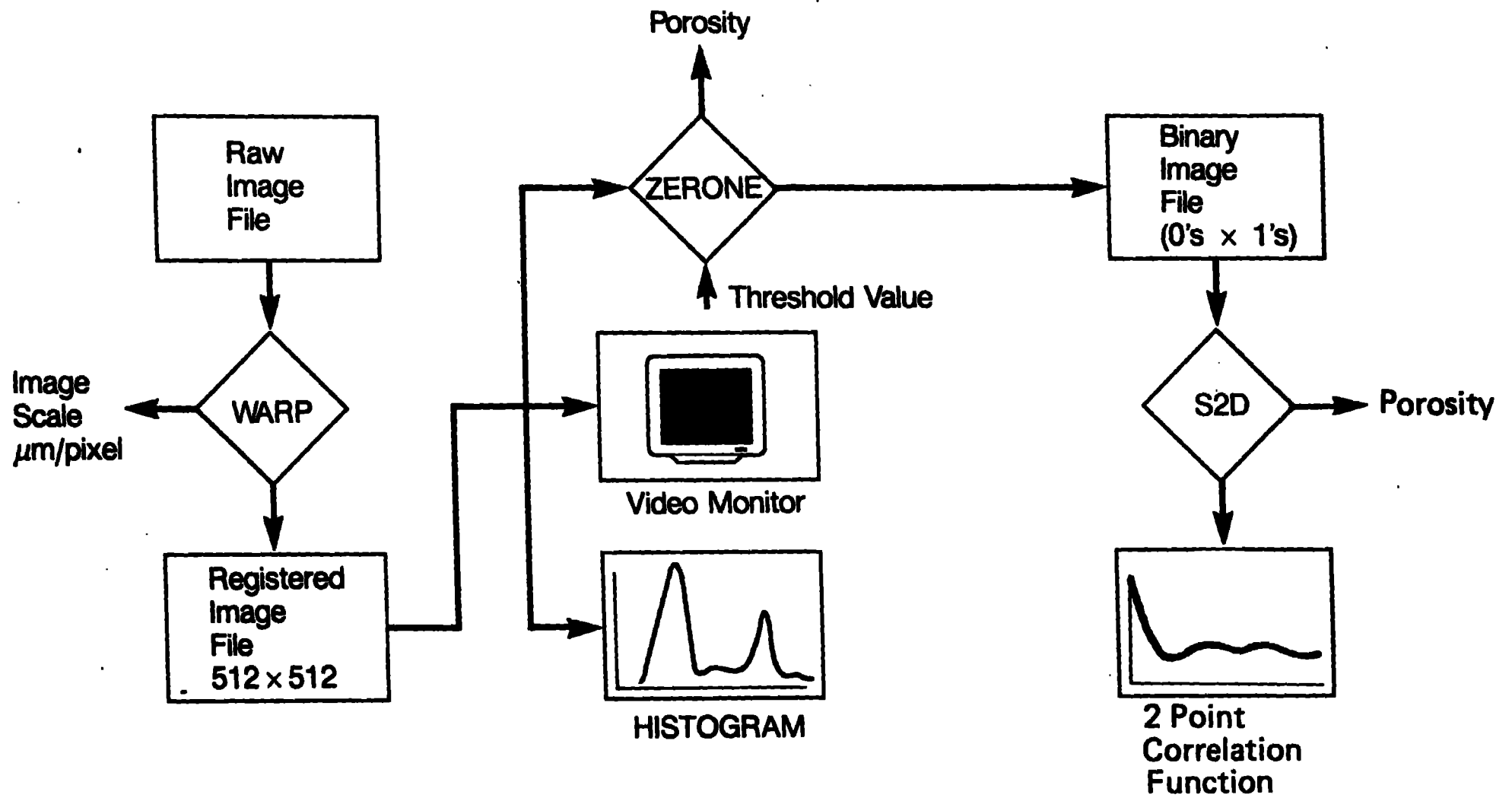
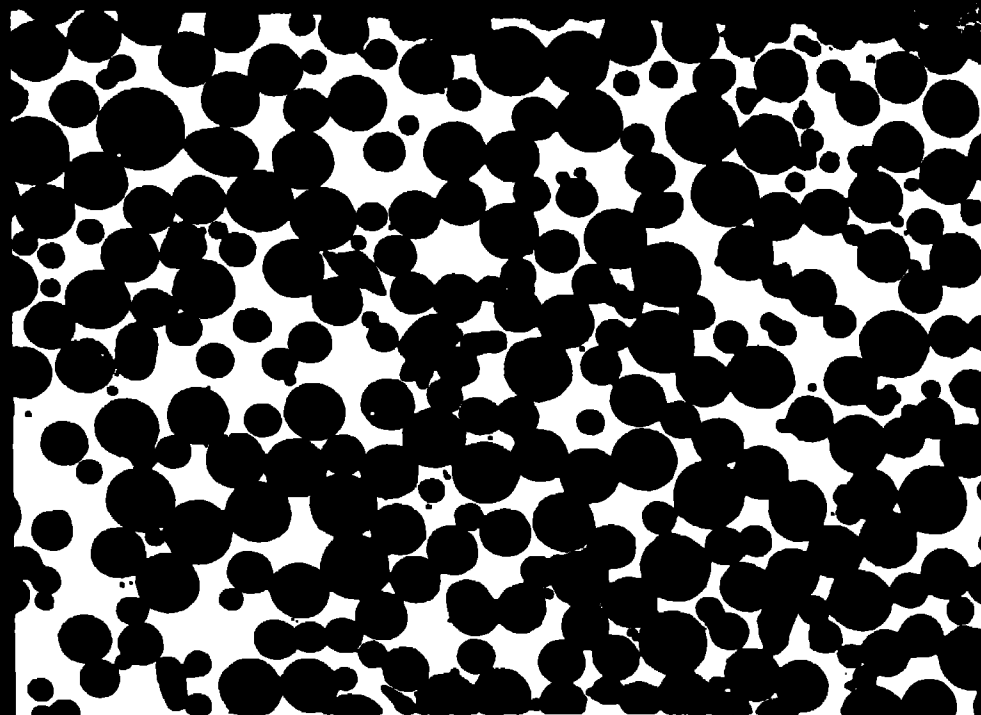


Figure 4a



20KV X50 1000U 004 00055 EP

Figure 16

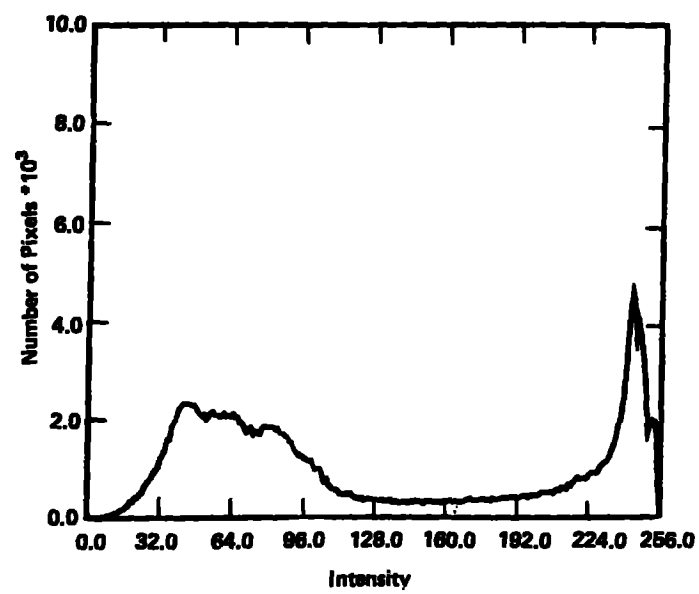


Figure 4c

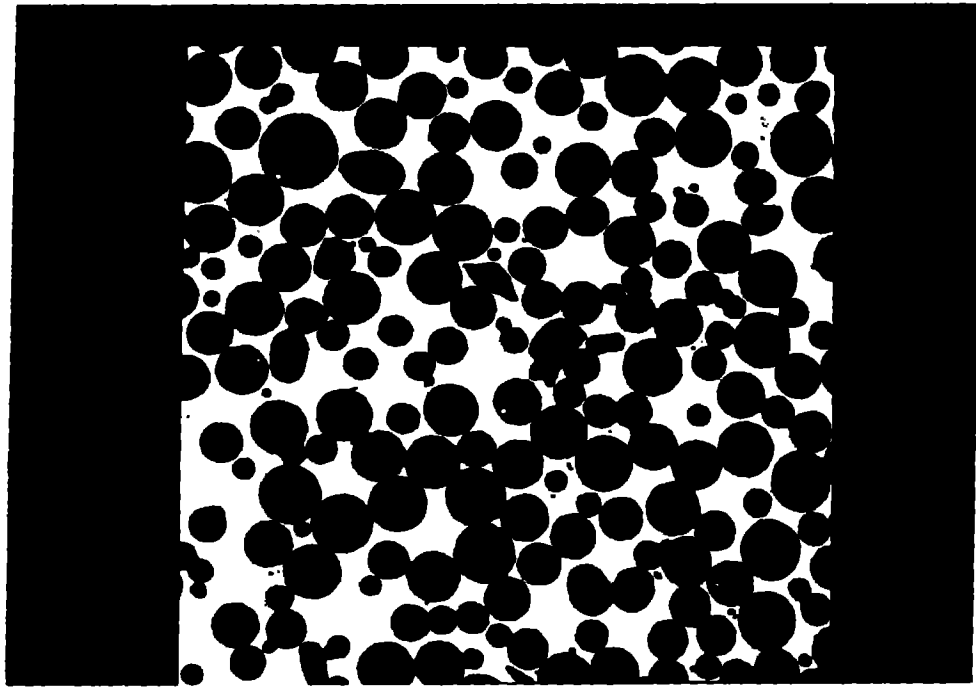


Figure 4d

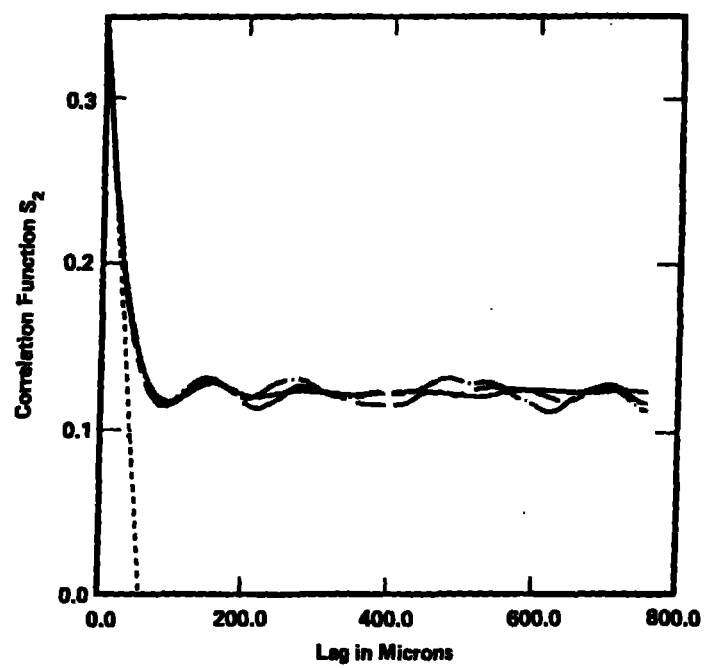


Figure 5a

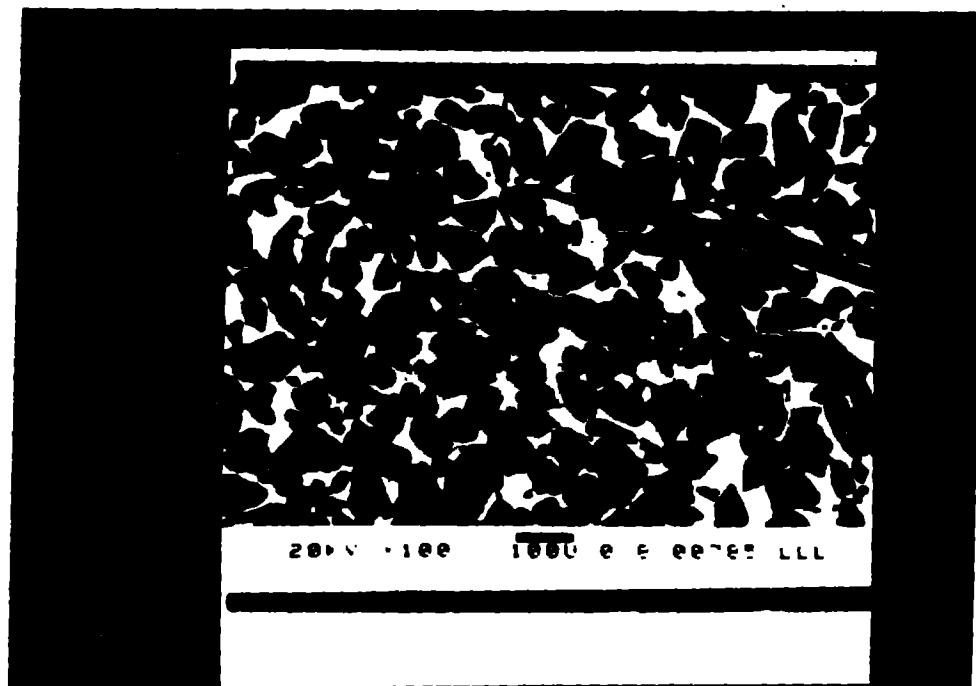
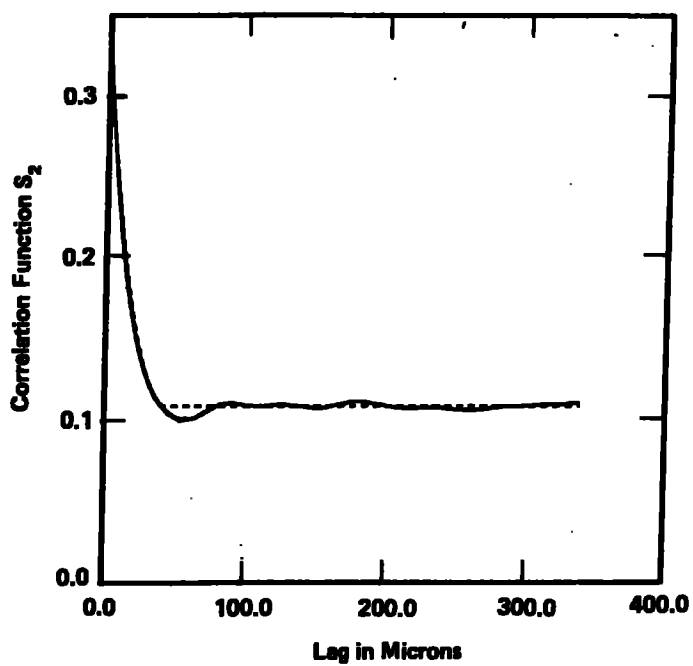


Figure 5b



IG-785-212

Figure 6a

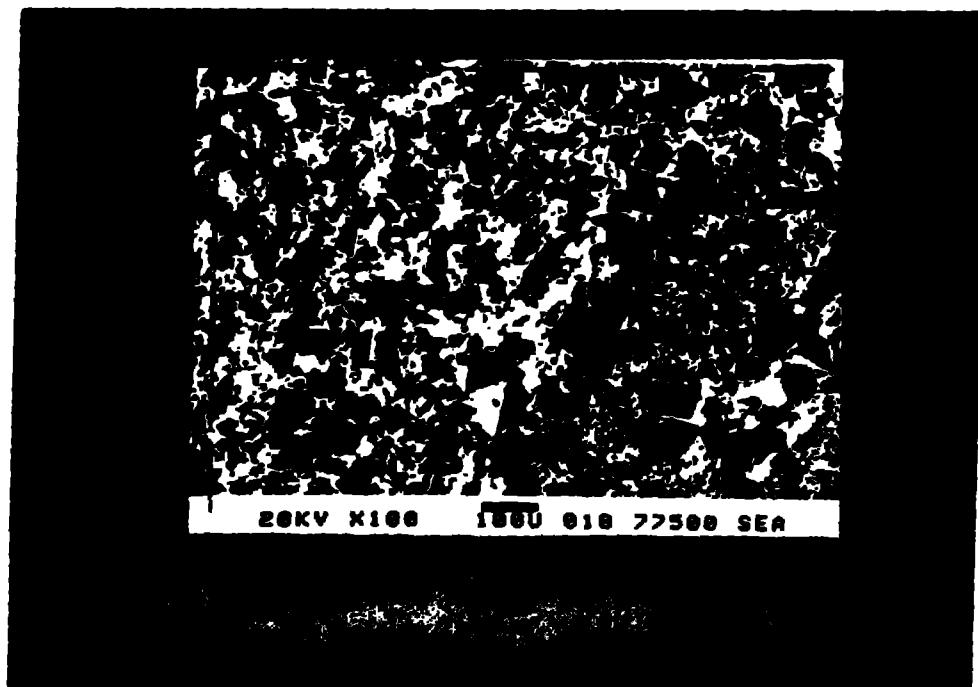


Figure 6b

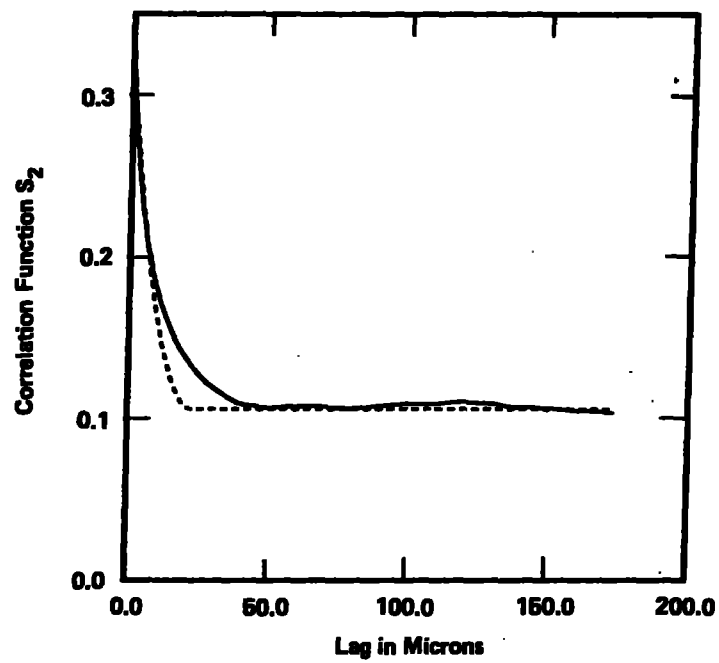


Figure 7a



Figure 7b

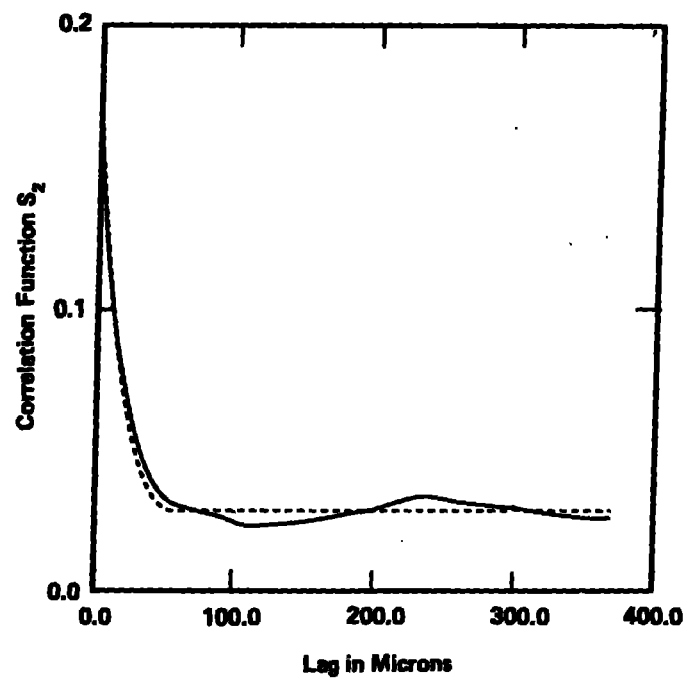


Figure 8a

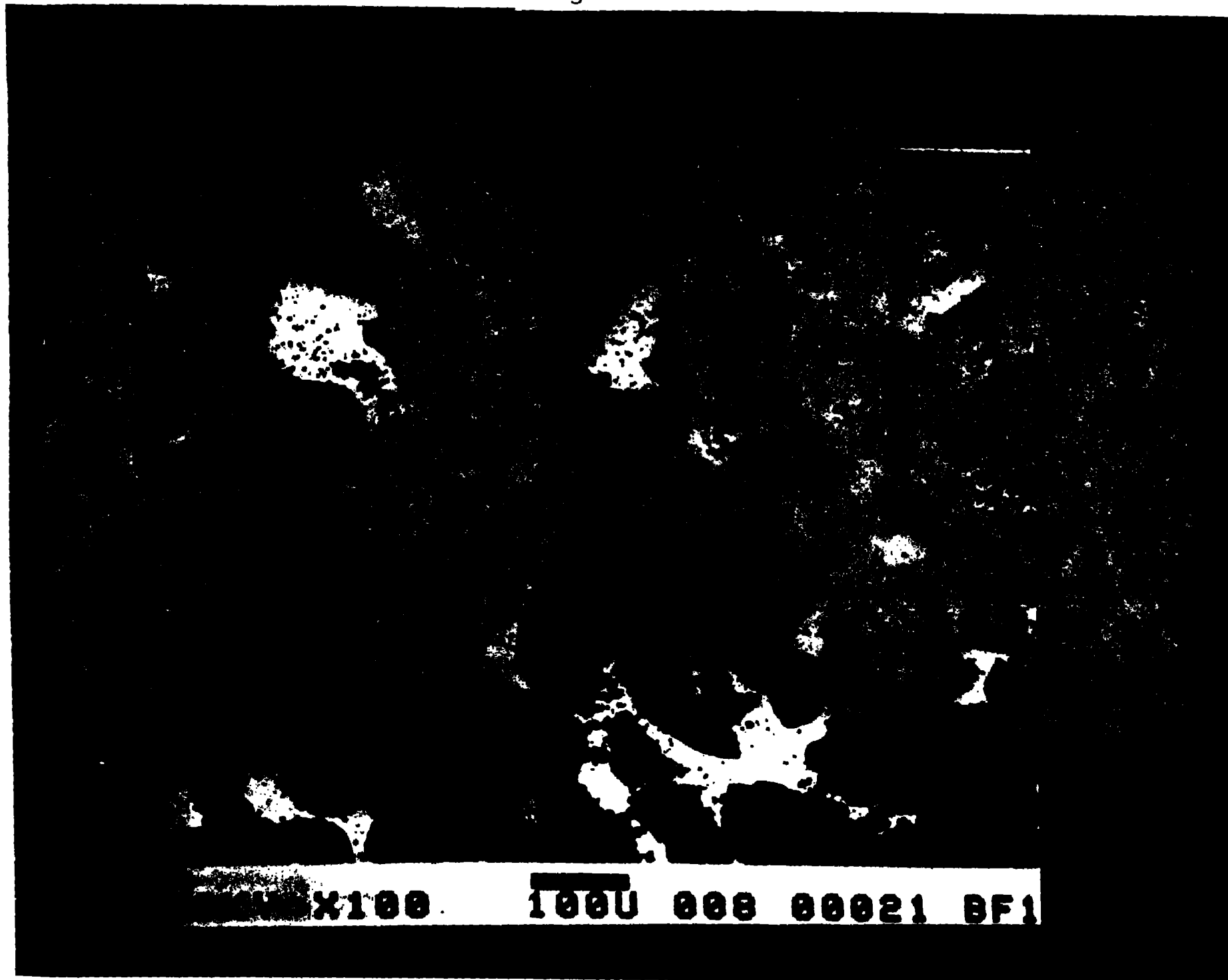


Figure 6b

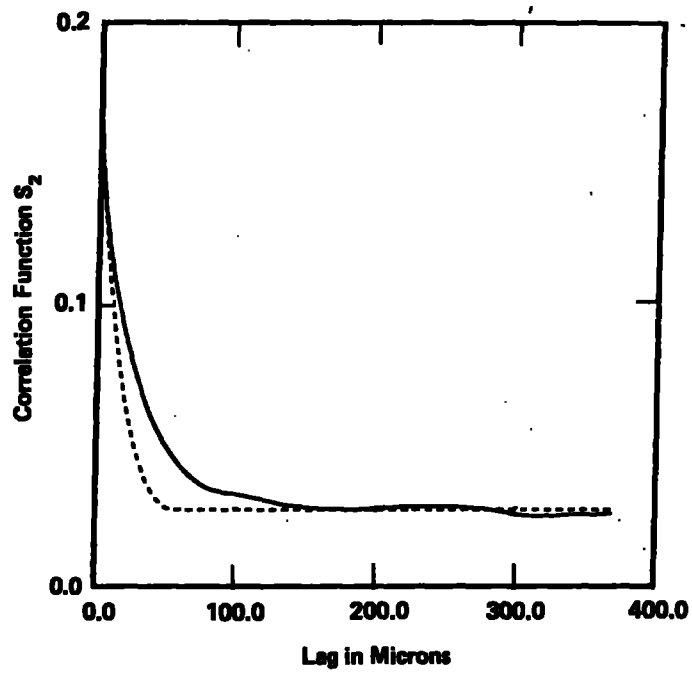


Figure 9a



20KV X490 100U 000 00000 BF1

Figure 1b

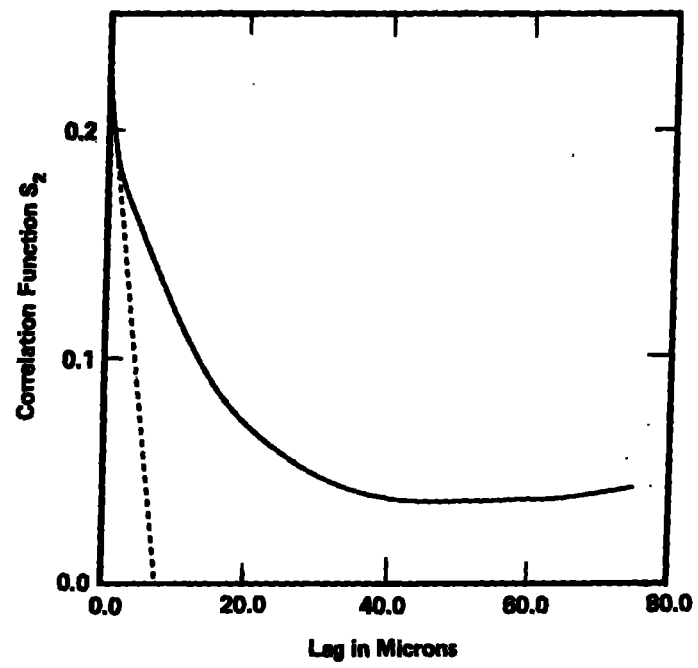


Figure 10a

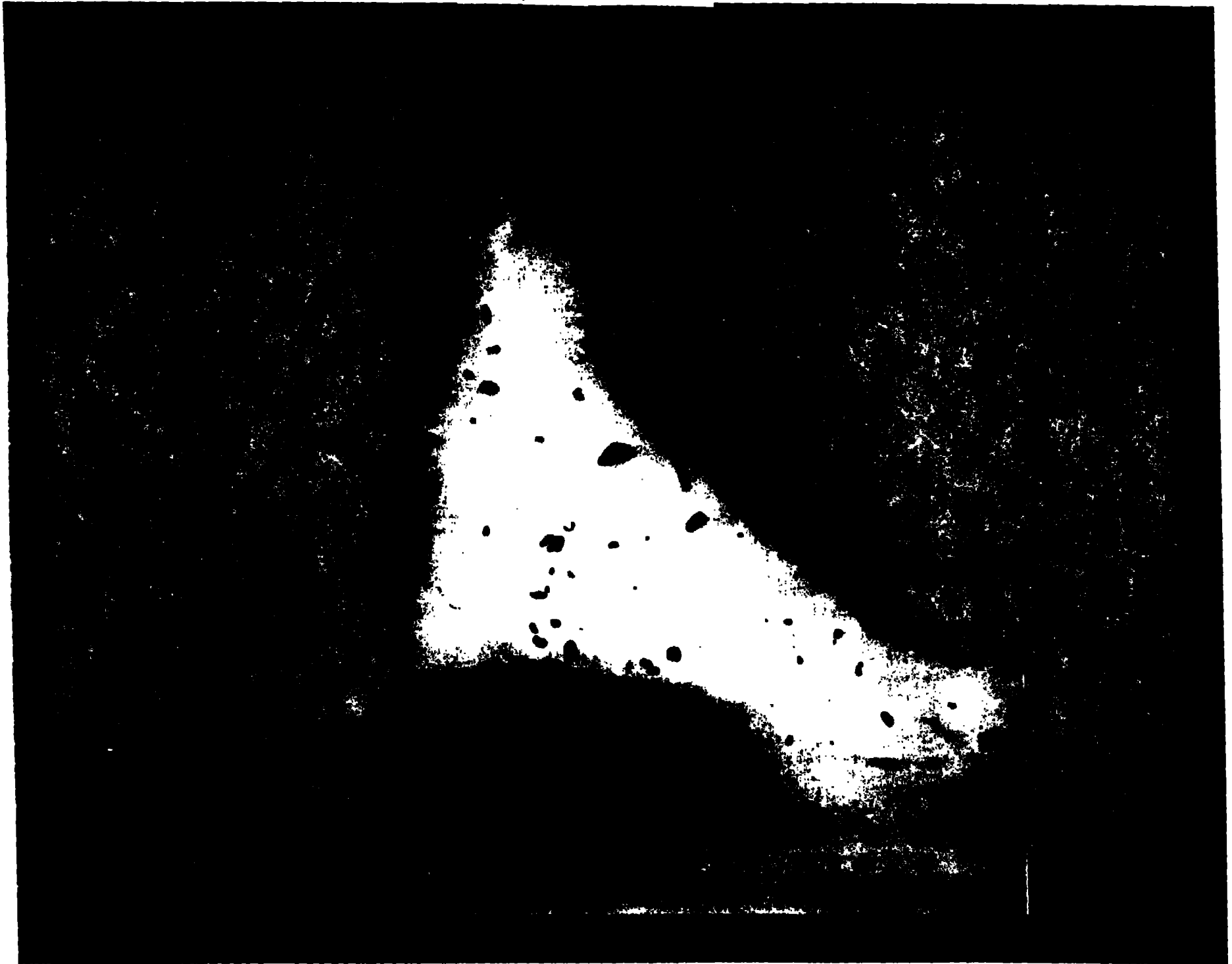


Figure 106

